



1 **Advances in Land Surface Model-based Forecasting: A**
2 **Comparison of LSTM, Gradient Boosting, and Feedforward**
3 **Neural Networks as Prognostic State Emulators in a Case Study**
4 **with ECLand**

5

6 Marieke Wesselkamp¹, Matthew Chantry², Ewan Pinnington², Margarita Choulga², Souhail Boussetta², Maria

7 Kalweit³, Joschka Boedecker^{3,4}, Carsten F. Dormann¹, Florian Pappenberger², and Gianpaolo Balsamo^{2,5}

8

9

10 ¹ Department of Biometry, University of Freiburg, Germany

11 ² European Centre for Medium-Range Weather Forecasts, Reading, United Kingdom

12 ³ Department of Computer Science, University of Freiburg, Germany

13 ⁴ BrainLinks-BrainTools, University of Freiburg, Germany

14 ⁵ World Meteorological Organization, Geneva, Switzerland

15

16

17 Correspondence to: Marieke Wesselkamp (marieke.wesselkamp@biom.uni-freiburg.de)

18



19

Abstract

20

21 Most useful weather prediction for the public is near the surface. The processes that are most
22 relevant for near-surface weather prediction are also those that are most interactive and
23 exhibit positive feedback or have key role in energy partitioning. Land surface models
24 (LSMs) consider these processes together with surface heterogeneity and forecast water,
25 carbon and energy fluxes, and coupled with an atmospheric model provide boundary and
26 initial conditions. This numerical parametrization of atmospheric boundaries being
27 computationally expensive, statistical surrogate models are increasingly used to accelerated
28 progress in experimental research. We evaluated the efficiency of three surrogate models in
29 speeding up experimental research by simulating land surface processes, which are integral to
30 forecasting water, carbon, and energy fluxes in coupled atmospheric models. Specifically, we
31 compared the performance of a Long-Short Term Memory (LSTM) encoder-decoder
32 network, extreme gradient boosting, and a feed-forward neural network within a physics-
33 informed multi-objective framework. This framework emulates key states of the ECMWF's
34 Integrated Forecasting System (IFS) land surface scheme, ECLand, across continental and
35 global scales. Our findings indicate that while all models on average demonstrate high
36 accuracy over the forecast period, the LSTM network excels in continental long-range
37 predictions when carefully tuned, the XGB scores consistently high across tasks and the MLP
38 provides an excellent implementation-time-accuracy trade-off. The runtime reduction
39 achieved by the emulators in comparison to the full numerical models are significant, offering
40 a faster, yet reliable alternative for conducting numerical experiments on land surfaces.

41



42 **1 Introduction**

43

44 While forecasting of climate and weather system processes has long been a task for numerical
45 models, the recent development in deep learning has introduced competitive machine-
46 learning (ML) systems for numerical weather prediction (NWP) (Bi et al., 2022; Lam et al.,
47 2023), (Lang et al., 2024). Land surface models (LSMs), even though being an integral
48 part of numerical weather prediction, have not yet caught the attention of the ML-
49 community. LSMs forecast water, carbon and energy fluxes, and in coupling with
50 an atmospheric model, provide the lower boundary and initial conditions [3], [4]. The
51 parametrization of land surface states thus does not only affect predictability of earth and
52 climate systems on sub-seasonal scales (Muñoz-Sabater et al., 2021), but also the short- and
53 medium-range skill of NWP forecasts (De Rosnay et al., 2014). Beyond the online integration
54 with NWPs, offline versions of LSMs provide research tools for experiments on the land
55 surface (Boussetta et al., 2021), the diversity of which are however limited by the required
56 substantial computational resources and often moderate runtime efficiencies (Reichstein et
57 al., 2019).

58 Emulators constitute statistical surrogates for numerical simulation models that, by
59 approximating the latter, aim at increasing computational efficiency (Machac et al., 2016).

60 While for construction emulators can themselves require substantial computational
61 resources, their subsequent evaluation usually runs orders of magnitude faster than the
62 original numerical model (Fer et al., 2018). For this reason, emulators have found application
63 for example in modular parametrization of online weather forecasting systems (Chantry et al.,
64 2021), in replacing the MCMC-sampling procedure in Bayesian calibration of ecosystem
65 models (Fer et al., 2018), or in generating ensembles of atmospheric states for forecast
66 uncertainty quantification (Li et al., 2023). Beyond their computational efficiency, surrogate
67 models with high parametric flexibility have the potential to correct for process mis-
68 specification and improve predictions towards a physical model (Wesselkamp et al., 2022).
69 Modelling approaches used for emulation range from low parametrized, auto-regressive
70 linear models to highly non-linear and flexible neural networks (Nath et al., 2022), (Baker et
71 al., 2022), (Chantry et al., 2021), (Meyer et al., 2022). In the global land surface system M-
72 MESMER, a set of simple AR1 regression models is used to initialize the numerical LSM,
73 resulting in a modularized emulator (Nath et al., 2022). Numerical forecasts of gross primary
74 productivity and hydrological targets were successfully approximated by Gaussian processes



75 (Baker et al., 2022)(Machac et al., 2016), the advantage of which is their direct quantification
76 of prediction uncertainty. When it comes to highly diverse or structured data, neural networks
77 have shown to deliver accurate approximations for variables from gravity wave drags to
78 urban surface temperature (Chantry et al., 2021)(Meyer et al., 2022). In most fields of
79 machine learning, specific types of neural networks are now the best approach to representing
80 fit and prediction. One exception is so-called tabular data, i.e. data without spatial or temporal
81 interdependencies (as opposed to vision and sound), where extreme gradient boosting is still
82 the go-to approach (Grinsztajn et al., 2022; Shwartz-Ziv & Armon, 2021).

83 ECLand is the land surface scheme that provides boundary and initial conditions for the
84 Integrated Forecasting System (IFS) of the European Centre for Medium-range Weather
85 Forecasts (ECMWF) (Boussetta et al., 2021). Driven by meteorological forcing and spatial
86 climate fields, it has a strong influence on the NWP [5] and also constitutes a standalone
87 framework for offline forecasting of land surface processes, the advantage of which for the
88 online framework is the temporal consistency of prognostic state variables (Muñoz-Sabater et
89 al., 2021). The modular construction of ECLand offers potential for element-wise
90 improvement of process representation and thus a stepwise development towards increased
91 computational efficiency. Within the IFS, ECLand also forms the basis of the land surface
92 data assimilation system, updating the land surface state with synoptic data and satellite
93 observations of soil moisture and snow. Emulators of physical systems have been shown to
94 be beneficial in data assimilation routines, allowing for a quick and low maintenance
95 estimation of the tangent linear model (Hatfield et al., 2021). Together with the potential to
96 run large ensembles of land surface states at a much-reduced cost, this would be a potential
97 application of the surrogate models introduced here.

98 Long-short term memory networks (LSTMs) have gained popularity in hydrological
99 forecasting as rainfall-runoff models, for predicting stream flow temperature and also soil
100 moisture [e.g. (Kratzert, Klotz, et al., 2019), (Lees et al., 2022), (Zwart et al., 2023), (Bassi
101 et al., 2024)]. Research on the interpretability of LSTMs has found correlations between the
102 model cell states and spatially or thematically similar hydrological units (Lees et al., 2022),
103 suggesting the specific usefulness of LSTM for representing variables with dynamic storages
104 and reservoirs (Kratzert, Herrnegger, et al., 2019). As emulators, LSTMs have been shown
105 useful for sea surface level projection in a variational manner with Monte Carlo dropout (Van
106 Katwyk et al., 2023). While most of these studies trained their models on observations or
107 reanalysis data, our emulator learns the representation from ECLand simulations directly. To



108 our knowledge, a comparison of models without memory mechanisms to an LSTM-based
109 neural network for global land surface emulation has not been conducted before.
110 We emulate seven prognostic state variables of ECLand, which represent core land surface
111 processes: soil water volume and soil temperature, each at three depth layers, and snow cover
112 fraction at the surface layer. These three state variables represent the core of the current
113 configuration of ECLand We specifically focus on the utility of memory mechanisms,
114 highlighting the development of a single LSTM-based encoder-decoder model compared to
115 an extreme gradient boosting approach (XGB) and a multilayer perceptron (MLP), which all
116 perform the same tasks. The LSTM architecture builds on an encoder-decoder network design
117 introduced for flood forecasting (Nearing et al., 2024). To compare forecast skill
118 systematically, the three emulators were compared in long-range forecasting against
119 climatology (Pappenberger et al., 2015). In this work, evaluation is done on ECLand
120 simulation only, i.e. on purely synthetic data, while future work will encompass transfer
121 learning and validation on observations.

122

123 **2 Methods**

124

125 **2.1 The Land Surface Model: ECLand**

126

127 ECLand is a tiled ECMWF Scheme for Surface Exchanges over Land that represents surface
128 heterogeneity and incorporates land surface hydrology (ECLand) (Balsamo et al., 2011)
129 (ECMWF, 2017). ECLand computes surface turbulent fluxes (of heat, moisture and
130 momentum) and skin temperature over different tiles (vegetation, bare soil, snow,
131 interception and water) and then calculates an area-weighted average for the grid-box to
132 couple with the atmosphere (Boussetta et al., 2021). For the overall accuracy of the model,
133 accurate parameterizations are essential (Kimpson et al., 2023) as e.g. the land surface
134 parameterization determines the sensible and latent heat fluxes, and provide the lower
135 boundary conditions for enthalpy and moisture equations in the atmosphere (Viterbo, 2002).
136 We emulate three prognostic state variables of ECLand, that represent core land surface
137 processes: soil water volume and soil temperature at each three depth layers (each at 0 – 7
138 cm, 7 – 21 cm and 21 – 72 cm) and snow cover fraction, aggregated at the surface layer, so
139 below are some more details on these parametrisations.

140



141 **2.2 Data sources**

142

143 As training data base, global simulation and reanalysis time series from 2010 to 2022 were
144 compiled to *zarr* format at an aggregated 6-hourly temporal resolution. Simulations and
145 climate fields were generated from ECMWFs development cycle CY49R2, ECLand forced by
146 ERA-5 meteorological reanalysis data (Hersbach et al., 2020).

147 There are three main sources of data used for creation of the data base: The first is a selection
148 of surface physiographic fields from ERA5 (Hersbach et al., 2020) and their updated versions
149 (Choulga et al., 2019), (Boussetta et al., 2021), (Muñoz-Sabater et al., 2021) used as static
150 model input features (X). The second is a selection of atmospheric and surface model fields
151 from ERA5, used as static and dynamic model input features (Y). The third is ECLand
152 simulation results, constituting the model's dynamic prognostic state variables (z) and hence
153 model input and target features. A total of 41 static, seasonal and dynamical features were
154 used to create the emulators, see table 1 for an overview of input variables and details on the
155 surface physiographic and atmospheric fields below.

156

157 **2.2.1 Surface physiographic fields**

158

159 Surface physiographic fields have gridded information of the Earth's surface properties (e.g.
160 land use, vegetation type, and distribution) and represent surface heterogeneity in the ECLand
161 of the IFS (Kimpson et al., 2023). They are used to compute surface turbulent fluxes (of heat,
162 moisture, and momentum) and skin temperature over different surfaces (vegetation, bare soil,
163 snow, interception, and water) and then to calculate an area-weighted average for the grid box
164 to couple with the atmosphere. To trigger all different parametrization schemes, the ECMWF
165 model uses a set of physiographic fields that do not depend on initial condition of each
166 forecast run or the forecast step. Most fields are constant; surface albedo is specified for 12
167 months to describe the seasonal cycle. Depending on the origin, initial data come at different
168 resolutions and different projections and are then first converted to a regular latitude–
169 longitude grid (EPSG:4326) at ~ 1 km at Equator resolution and secondly to a required grid
170 and resolution. Surface physiographic fields used in this work consist of orographic, land,
171 water, vegetation, soil, albedo fields, see Table 1 for the full list of surface physiographic
172 fields; for more details, see IFS documentation (ECMWF, 2023).

173

174 **2.2.2 ERA5**



175

176 Climate reanalyses combine observations and modelling to provide calculated values of a
 177 range of climactic variables over time. ERA5 is the fifth-generation reanalysis from
 178 ECMWF. It is produced via 4D-Var data assimilation of the IFS cycle 41R2 coupled to a land
 179 surface model (ECLand, (Boussetta et al., 2021)), which includes lake parametrization by
 180 Flake (Mironov & Helmert, n.d.) and an ocean wave model (WAM). The resulting data
 181 product provides hourly values of climatic variables across the atmosphere, land, and ocean
 182 at a resolution of approximately 31 km with 137 vertical sigma levels up to a height of 80 km.
 183 Additionally, ERA5 provides associated uncertainties of the variables at a reduced 63 km
 184 resolution via a 10-member ensemble of data assimilations. In this work, ERA5 hourly
 185 surface fields at ~ 31 km resolution on the cubic octahedral reduced Gaussian grid (i.e.
 186 Tco399) are used. The Gaussian grid’s spacing between latitude lines is not regular, but lines
 187 are symmetrical along the Equator; the number of points along each latitude line defines
 188 longitude lines, which start at longitude 0 and are equally spaced along the latitude line. In a
 189 reduced Gaussian grid, the number of points on each latitude line is chosen so that the local
 190 east–west grid length remains approximately constant for all latitudes (here, the Gaussian
 191 grid is N320, where N is the number of latitude lines between a pole and the Equator).

192

193 *Table 1 Input and target features to all emulators from the data sources. The left column shows the observation-derived static*
 194 *physiographic fields, the middle column ERA5 dynamic physiographic and meteorological fields and the rightmost column*
 195 *ECLand generated dynamic prognostic state variables.*

| Climate fields | Units | Atmospheric forcing | Units | Prognostic states | Units |
|--|-------|---|------------------|---|--------------------------------|
| Vegetation cover (<i>low, high</i>) | | Total precipitation fraction (<i>convective + stratiform</i>) | | Soil water volume (<i>Layers 1-3</i>) | m ³ m ⁻³ |
| Type of vegetation (<i>low, high</i>) | | Downward radiation (<i>long, short</i>) | W/m ² | Soil temperature (<i>Layers 1-3</i>) | K |
| Minimum stomatal resistance (<i>low, high</i>) | | Seasonal LAI (<i>high, low</i>) | | Snow cover fraction | |
| Roughness length (<i>low, high</i>) | | Wind speed (<i>v, u</i>) | m/s | | |
| Urban cover | | Surface pressure | Pa | | |
| Lake cover | | Skin temperature | K | | |
| Lake depth | | | | | |



| | | | |
|---|------------|--------------------------------|--------|
| Orography (+ <i>std.</i> + <i>filtered</i>) | m2/s- 2 | Specific humidity | kg/kg |
| Photosynthesis pathways | | Rainfall rate (<i>total</i>) | kg/m2s |
| Soil type | | Snowfall rate (<i>total</i>) | kg/m2s |
| Glacier mask | | | |
| Permanent wilting point | | | |
| Field capacity | | | |
| Cell area | | | |

196

197 **2.3 Emulators**

198

199 We compare the utility of a long-short term memory neural network (LSTM), that of extreme
 200 gradient boosting regression trees (XGB) and that of a feedforward neural network (that we
 201 here refer to as multilayer perceptron, MLP). To motivate this setup and pave the way for
 202 discussing effects of (hyper-)parameter choices, a short overview of all approaches is given.
 203 All analyses were conducted in Python. XGB was developed in dmlc’s XGBoost python
 204 package¹. The MLP and LSTM were developed in the PyTorch lightning framework for deep
 205 learning². Neural networks were trained with the Adam algorithm for stochastic optimization
 206 (Kingma & Ba, 2017). Model architectures and algorithmic hyperparameters were selected
 207 through Bayesian hyperparameter optimization with the Optuna framework (Akiba et al.,
 208 2019). The Bayesian optimization minimizes the neural network validation accuracy,
 209 specified here as mean absolute error (MAE), over a predefined search space for free
 210 hyperparameters with the Tree-structured Parzen Estimator (Ozaki et al., 2022). The resulting
 211 hyperparameter and architecture choices which were used for the different approaches are
 212 listed in the Supplementary Material.

213

214 **2.3.1 MLP**

215

216 For creation of the MLP emulator we work with a feed-forward neural network architecture
 217 of connected hidden layers with ReLU activations and dropout layers, model components
 218 which are given in detail in the Supplementary Material or in (Goodfellow et al., 2016). The

¹ <https://xgboost.readthedocs.io/en/stable/python/index.html>

² <https://lightning.ai/docs/pytorch/stable/>



219 MLP was trained with a learning rate scheduler. L2-regularization was added to the training
220 objective via weight decay. Sizes and width of hidden layers as well as hyperparameters were
221 selected together in the hyperparameter optimization procedure. Instead of forecasting
222 absolute prognostic state variables \mathbf{z}_t , the MLP predicts the 6-hourly increment, $\frac{\widehat{d\mathbf{z}}}{dt}$. It is
223 trained on a stepwise rollout prediction of future state variables at a pre-defined lead time at
224 given forcing conditions, see details in the section on optimization.

225

226 2.3.2 LSTM

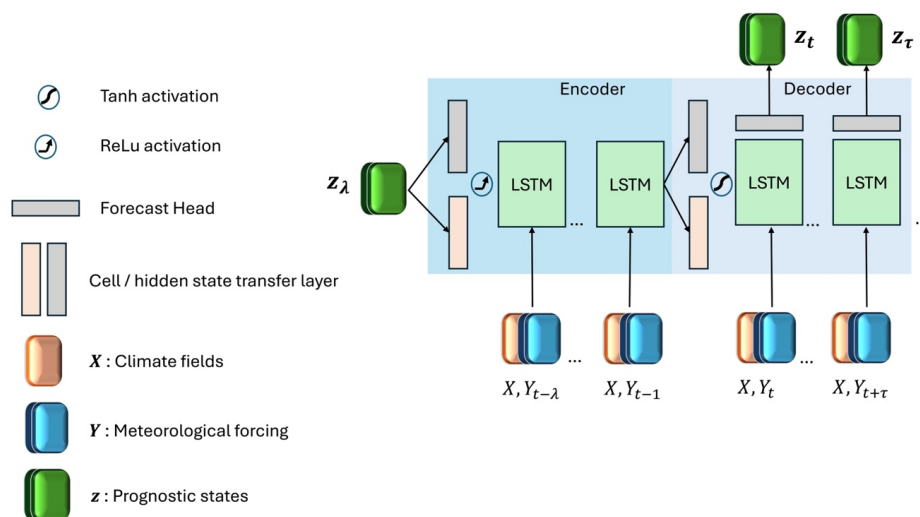
227

228 LSTMs are recurrent networks that consider long-term dependencies in time series through
229 gated units with input and forget mechanisms (Hochreiter & Schmidhuber, 1997). In
230 explicitly providing time-varying forcing and state variables, LSTM cell states serve as long-
231 term memory while LSTM hidden states are the cells' output and pass on stepwise short-term
232 representations stepwise. In short notation (Lees et al., 2022), a one-step ahead forward pass
233 followed by a linear transformation can be formulated as

$$234 \quad \mathbf{h}_t, \mathbf{c}_t = f(\mathbf{x}_t, \mathbf{h}_{t-1}, \mathbf{c}_{t-1}, \boldsymbol{\theta})$$

$$235 \quad \hat{\mathbf{z}}_t = \mathbf{A}\mathbf{h}_t + b$$

236 where \mathbf{h}_{t-1} denotes the hidden state, i.e. output estimates from the previous time step, \mathbf{c}_{t-1}
237 the cell state from the previous time step, and $\boldsymbol{\theta}$ the time-invariant model weights. We stacked
238 multiple LSTM cells to an encoder-decoder model with transfer layers for hidden and cell
239 state initialization and for transfer to the context vector (see figure 1) (Nearing et al., 2024). A
240 lookback l of the previous static and dynamic feature states are passed sequentially to the first
241 LSTM cells in the encoder layer, while the l prognostic state variables \mathbf{z} initialize the hidden
242 state \mathbf{h}_0 after a linear embedding. The output of the first LSTM layer cells become the input
243 to the deeper LSTM layer cells and the last hidden state estimates are the final output from
244 the encoder. Followed by a non-linear transformation with hyperbolic tangent activation, the
245 hidden cell states are transformed into a weighted context vector \mathbf{s} . Together with the encoder
246 the cell state (\mathbf{c}_t, \mathbf{s}) initializes the hidden and cell states of the decoder. The decoder LSTM
247 cells take as input again static and dynamic features sequentially at lead times $t = 1, \dots, \tau$, but
248 not the prognostic states variables. These are estimated from the sequential hidden states of
249 the last LSTM layer cells, transformed to target size with a linear forecast head before
250 prediction. LSTM predicts absolute state variables \mathbf{z}_t while being optimized on \mathbf{z}_t and $d\hat{\mathbf{z}}_t$
251 simultaneously, see section on optimization.



252

253 *Figure 1: LSTM architecture. Blue shaded area indicates the encoder part, where the model is driven by a lookback λ*
 254 *of meteorological forcing and state variables. The light-blue shaded area indicates the decoder part that is initialized*
 255 *from the encoding to unroll LSTM forecasts from the initial time step t up to a flexibly long lead time of τ .*

256 **2.3.3 XGB**

257

258 Extreme gradient boosting (XGB) is a regression tree ensemble method that uses an
 259 approximate algorithm for best split finding. It computes first and second order gradient
 260 statistics in the cost function, performing a similar to gradient descent optimization (T. Chen
 261 & Guestrin, 2016), where each new learner is trained on the residuals of the previous ones.
 262 Regularization and column sampling aim for preventing overfitting internally. XGB is known
 263 to provide a powerful benchmark for time series forecasting and tabular data [(T. Chen &
 264 Guestrin, 2016; Shwartz-Ziv & Armon, 2021), (X. Chen et al., 2020)]. Like the MLP, it is
 265 trained to predict the increment $\widehat{\Delta z}_{t,i}$ of prognostic state variables, but only for a one-step
 266 ahead prediction.

267

268 **2.4 Experimental setup**

269

270 We distinguish the experimental analysis into three parts that vary in the usage of the training
 271 database: (1) model development, (2) model testing, and (3) global model transfer.
 272 The models were developed and for the first time evaluated on a low state resolution
 273 (ECMWF’s TCO199 reduced gaussian grid, see section on data sources) and temporal subset
 274 from the training data base, i.e. on a bounding box of 7715 grid cells over Europe with time



275 series of six years from 2016 to 2022. For details on the development data base, model
276 selection and model performances, see Supplementary Material S3.
277 The selected models were recreated on a high state resolution (TCO399) continental scale
278 European subset with 10 051 grid cells. Models were trained on five years 2015-2020 with
279 the year 2020 as validation split and evaluated on the year 2021 for the scores we report in
280 the main part. Note that for computation of forecast horizons, the two test years 2021 and
281 2022 were used, see details in section on forecast horizons. With this same data splitting
282 setup, the analysis was repeated in transferring the candidates to the low resolution (TCO199)
283 global data set with a total of 47892 grid cells. The low global resolution on one hand allowed
284 a systematic comparison of the three models, because high resolution training with XGB was
285 prohibited by the required working memory. On the other hand, this extrapolation scenario
286 created an unseen problem for the models that were selected on a continental and high-
287 resolution scale which is reflected in the resulting scores.

288

289 **2.5 Optimization**

290

291 **2.5.1 Loss functions**

292

293 The basis of the loss function \mathcal{L} for the neural network optimization was PyTorch's
294 SmoothL1Loss³, a robust loss function that combines L1-norm and L2-norm and is less
295 sensitive to outliers than pure L1-norm (Girshick, 2015). Based on a pre-defined threshold
296 parameter β , smooth L1 transitions from L2-norm to L1-norm above the threshold.
297 SmoothL1Loss \mathcal{L} is defined as

$$298 \quad \mathcal{L}(\hat{z}, z) = 0.5(\hat{z} - z)^2 \frac{1}{\beta} \text{ if } |\hat{z} - z| < \beta \text{ and}$$

$$299 \quad \mathcal{L}(\hat{z}, z) = |\hat{z} - z| - 0.5 \beta \text{ otherwise,}$$

300 here with $\beta = 1$. All models were trained to minimize the incremental loss \mathcal{L}_s that is the
301 differences between the estimates of the seven prognostic states increments \widehat{dz}_t and the full
302 model's prognostic states increments dz_t simultaneously as the sum of losses over all states.
303 We opted for a loss function equally weighted by variables to share inductive biases among
304 the non-independent prognostic states (Sener & Koltun, 2018). When aggregating over all
305 training lead times $t = 1, \dots, \tau$, \mathcal{L}_s and grid cells $i = 1, \dots, p$ is

³ <https://pytorch.org/docs/stable/generated/torch.nn.SmoothL1Loss.html>



306
$$\mathcal{L}_s(\widehat{d\mathbf{z}}, d\mathbf{z}) = \sum_t^\tau \sum_i^p \mathcal{L}_t(\widehat{d\mathbf{z}}_{t,i}, d\mathbf{z}_{t,i}),$$

307 Whereas when computing a rollout loss \mathcal{L}_r stepwise,

308

309
$$\mathcal{L}_r(\widehat{d\mathbf{z}}, \mathbf{z}) = \frac{1}{\tau} \sum_t^\tau \sum_i^p \mathcal{L}_t(z_{t-1,i} + \widehat{d\mathbf{z}}_{t,i}, z_{t,i})$$

310

311 Prognostic state increments are essentially the first differences from one to the next timestep
312 that are normalized again by the global standard deviation of the model's states increments,
313 s_{dz} before computation of the loss (Keisler, 2022). Due to the forecast models' structural
314 differences, loss functions were individually adapted:

315 **MLP** The combined loss function for the MLP is the sum of the incremental loss \mathcal{L}_s and the
316 rollout loss \mathcal{L}_r . For the rollout loss \mathcal{L}_r , \mathcal{L} was aggregated over grid cells p and accumulated
317 after an auto-regressive rollout over lead times τ , before being averaged out by division by τ
318 (Keisler, 2022).

319 **LSTM** The combined loss function for the LSTM is the sum of the incremental loss
320 \mathcal{L}_s , where the $d\widehat{\mathbf{z}}_t$ were derived from $\widehat{\mathbf{z}}_t$ after the forward pass, and the loss \mathcal{L} computed on
321 decoder estimates of prognostic states variables, a functionality that leverages the potential of
322 our LSTM structure.

323 **XGB** Trained only from one to the next time step, i.e. at a lead time of $\tau = 1$, the incremental
324 loss $\mathcal{L}_s = \mathcal{L}_r$. Without a SmoothL1Loss implementation provided in dmlc's XGBoost, we
325 trained XGB with both the Huber-Loss and the default L2-loss. The latter initially providing
326 better results, we chose the default L2-norm as loss function for XGB with the regularization
327 parameter $\lambda = 1$.

328

329 2.5.1 Normalization

330 As prognostic target variables are all lower bounded by zero, we tested both z-scoring and
331 max-scoring. The latter yielded no significant improvement, thus we show our results with z-
332 scored target variables. For neural network training but not for fitting XGB, static, dynamic
333 and prognostic state variables were all normalized with z-scoring towards the continental or
334 global mean \bar{z} and unit standard deviation s_z as

335
$$z_{t,n} = \frac{z_{t,n} - \bar{z}}{s_z}.$$



336 Prognostic target state increments were normalized again by the global standard deviation of
337 increments computing the loss (see section 2.5.1) to smooth magnitudes of increments
338 (Keisler, 2022). State variables were backtransformed to original scale before evaluation.

339

340 **2.5.3 Spatial and temporal sampling**

341 Sequences were sampled randomly from the training data set, while validation happened
342 sequentially. MLP and XGB were trained on all grid cells simultaneously in both the
343 continental and global setting, while LSTM was trained on the full continental data set but
344 was limited by GPU memory in the global task. We overcame this limitation by randomly
345 subsetting grid cells in the training data into largest possible, equally sized subsets which
346 were then loaded along with the temporal sequences during the batch sampling.

347

348 **2.6 Evaluation**

349

350 Three scores are used for model validation during the model development phase and in
351 validating architecture and hyperparameter selection, being the root mean squared error
352 (*RMSE*), the mean absolute error (*MAE*) and the anomaly correlation coefficient (*ACC*).
353 First, scores were assessed objectively in quantifying forecast accuracy of the emulators
354 against ECLand simulations directly with RMSE and MAE. Doing so, scores were
355 aggregated over lead times, grid cells or both. The total RMSE was computed as

$$356 \quad \text{RMSE} = \sqrt{\frac{\sum_{\tau,p}(z - \hat{z})^2}{n}},$$

357 As the mean absolute error in prognostic state variable prediction over the total of n grid cells
358 p times lead times τ . Equivalently, MAE was computed as

$$359 \quad \text{MAE} = \frac{\sum_{t,p} |z - \hat{z}|}{n},$$

360 Beyond accuracy, the forecast skill of emulators was assessed using a benchmark model: the
361 ACC (see below) as index of the long-term naïve climatology c of ECLand, forced by ERA5
362 (see section 2.2). More specifically, this is the 6-hourly mean of prognostic state variables
363 over the last 10 years preceding the test year, i.e. the years 2010 to 2020. While climatology
364 is a hard-to-beat benchmark specifically in long-term forecasting, the persistence is a
365 benchmark for short-term forecasting (Pappenberger et al., 2015). For verification against
366 climatology, we compute the anomaly correlation coefficient (*ACC*) over lead times as



367

$$ACC(t) = \frac{(\overline{\hat{z} - c})(\overline{z - c})}{\sqrt{(\overline{\hat{z} - c})^2 (\overline{z - c})^2}}$$

368 at each $t = 1, \dots, \tau$ where the overbar denotes averaging over grid cells $p = i, \dots, n$. The
369 nominator now indicates the mean squared skill error towards climatology and the
370 denominator its variability. ACC is bounded between 1 and -1, and an ACC of 1 indicates
371 perfect representation of forecast error variability, an ACC of 0.5 indicates a similar forecast
372 error to that of the climatology, an ACC of 0 indicates that forecast error variability
373 dominates and the forecast has no value and an ACC approaching -1 indicates that the
374 forecast has been very unreliable (ECMWF, n.d.). ACC is undefined when the denominator
375 is zero. This is the case either when mean squared emulator or ECLand anomaly, or both are
376 zero because forecast and climatology perfectly align, or because they cancel out at
377 summation to the mean.

378

379 **2.6.1 Forecast horizons**

380

381 Forecast horizons of the emulators are defined by the decomposition of the RMSE
382 (Bengtsson et al., 2008) into the emulator's variability around climatology (i.e. anomaly),
383 ECLand's variability around climatology and the covariance of both. The horizon is the point
384 in time at which the forecast error reaches saturation level, that is when the covariance of
385 emulator and ECLand anomalies approaches zero, as does the ACC.

386 We analysed predictive ability and predictability by computing the ACC for all lead times
387 from 6 hours to approx. one year, i.e. lead times $t = 1, \dots, \tau$, τ being 1350. As this confounds
388 the seasonality with the lead time, we compute these for every starting point of the prediction,
389 requiring two test years (2021 and 2022).

390 Forecast horizons based on the emulators' skill in standardized anomaly towards persistence
391 were equivalently computed but with persistence as a benchmark for shorter time scales, this
392 was only done for three months, from January to March 2021.

393 The analysis was conducted on two exemplary regions in northern and southern Europe that
394 represent very different conditions orography and in prognostic land surface states,
395 specifically in snow cover. For details on the regions and on the horizons computed with
396 standardized anomaly skill, see Appendices A1 and A4 respectively.

397

398 **3 Results**



399 **3.1 Aggregated performances**

400 **Europe.** All emulators approximated the numerical LSM with high average total accuracies
401 (all RMSEs < 1.58 and MAEs < 0.84) and confident correlations (all ACC > 0.72) (see table
402 2 and figure 2). The LSTM emulator achieved the best results across all total average scores
403 on the European scale. It decreased the total average MAE by ~25% towards XGB and by
404 ~37% towards the MLP and the total average RMSE by ~42% towards XGB and ~38%
405 towards the MLP. In total average ACC, the LSTM scored 20% higher than the MLP and
406 15% than XGB, also being the only emulator that achieved an ACC > 0.9. While the MLP
407 outperforms XGB in total average RMSE by ~5%, XGB scores better than the MLP in MAE
408 by ~27%.

409 At variable level, results differentiate into model specific strengths. In soil water volume,
410 XGB outperforms the neural network emulators by up to 60% in the first and second layer
411 MAEs towards the LSTM and up to over 40% for towards the MLP (see table 3). While the
412 representation of anomalies by specifically the LSTM decreases towards lower soil layers
413 with an ACC of only 0.6214 at the third soil layer, it remains consistently higher for XGB
414 with an ACC still > 0.789 at soil layer three.

415 In soil temperature approximation, LSTM achieves best accuracies at higher soil levels with
416 up to 7% improvement in MAE towards XGB and ACCs > 0.92, but XGB outperforms
417 LSTM at the third soil level with a close to 50% improvement (see table 4). The MLP doesn't
418 stand out by high scores on the continental scale. However, in terms of accuracy we found an
419 inverse ranking in the model development procedure during which LSTM outsourced XGB in
420 soil water volume but struggled with soil temperature approximations, for the interested
421 reader we refer to the supplementary information.

422 In snow cover approximation, the LSTM emulator enhances accuracies by over ~50% in
423 MAE towards both the XGB and the MLP emulator and scores highest in anomaly
424 representation with an ACC of ~0.87 compared to an ACC of ~0.66 for the MLP and only
425 ~0.74 for the XGB (see table 5).

426 **Globe.** Score ranking on the global scale varies strongly from the continental scale (see table
427 2). In total average accuracies, the MLP outperforms XGB by over 30% and LSTM by up
428 ~25% in RMSE and improves MAE more than 15% towards both. In anomaly correlation
429 however it scores last, whereas XGB achieves the highest total average of over 0.75.

430 Consistent with scores on the continental scale is XGBs high performance in soil temperature
431 (see table 3). It significantly outperforms the LSTM by ~60% in RMSE and nearly up to 75%
432 in MAE in all layers and the MLP by up to 50% in MAE at the top layer. Anomaly



433 persistence for all models degrade visibly towards the lower soil layers, while that of the
434 LSTM most relative to MLP and XGB. Similar to the continental scale, XGB also
435 outperforms the other candidates in soil temperature forecasts in all but the medium layer,
436 where the MLP gets higher scores in MAE and RMSE but not in ACC (see table 4). LSTM
437 doesn't stand out with any scores on the global scale.

438

439 **3.2 Spatial and temporal performances**

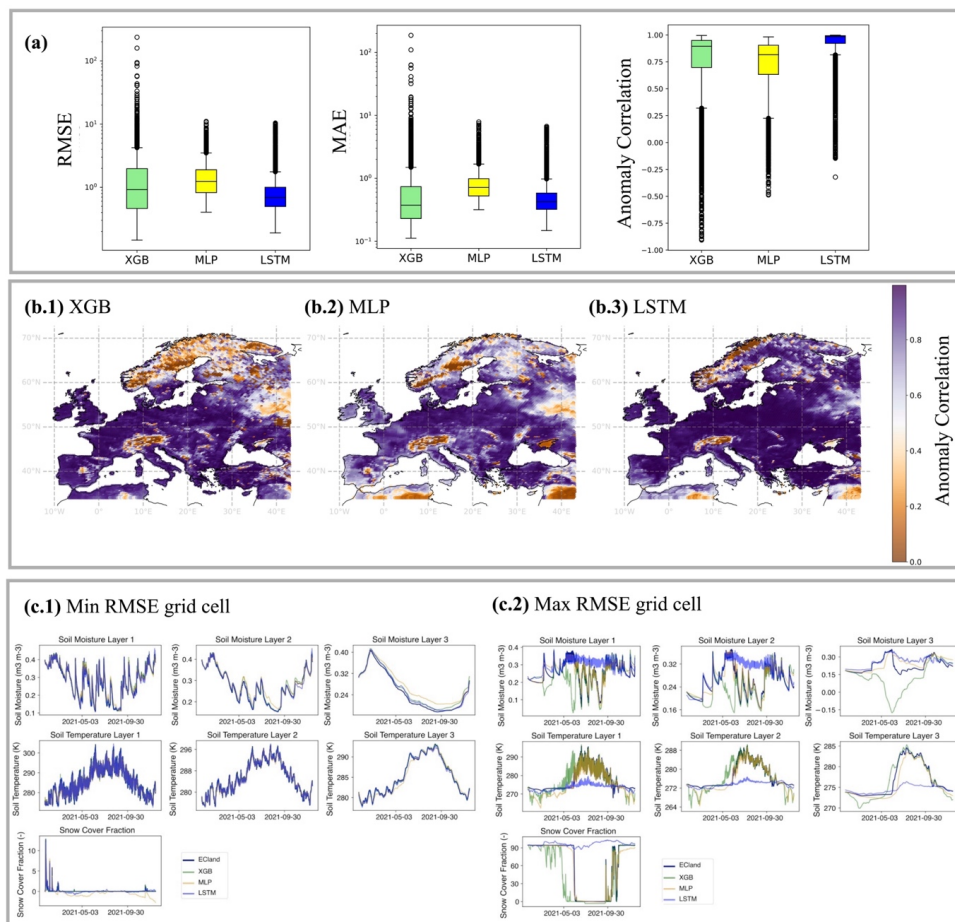
440

441 **Europe.** When summarizing temporally aggregated scores as boxplots to a total distribution
442 over space (see figure 2, A), the long tails of XGB scores become visible, whereas the MLP
443 indicates most robustness. This is reflected in the geographic distribution of scores at the
444 example of ACC (see figure 2, bottom), where the area of low anomaly correlation is largest
445 for XGB, ranging over nearly all northern Scandinavia, while MLP and LSTM have smaller
446 and more segregated areas of clearly low anomaly correlation. The LSTM shows a
447 homogeneously high ACCs over most of central Europe but the Alps, while also seems to be
448 challenged in areas of relative to the central Europe extreme weather conditions at the
449 Norwegian and Spanish coasts.

450 **Globe.** Similar to the results from the continental analysis, we find again long upper tails of
451 outliers for XGB in total spatial distribution of accuracies, both in RMSE and MAE and only
452 few outliers for MLP and LSTM. The anomaly correlation distribution changed towards
453 longer lower tails for MLP and LSTM and a shorter lower tail for XGB. We should, however,
454 take the results of total average ACC with care as it remains largely undefined in regions
455 without much noise in snow cover or soil water volume and globally represents mainly



456 patterns of soil temperature.



457

458 *Figure 2: a: Total aggregated distributions of (log) scores averaged over lead times, i.e. displaying the variation among*
 459 *grid cells. b: The distribution of the anomaly correlation in space on the European subset (b.1: XGB, b.2: MLP, b.3:*
 460 *LSTM). c: Model forecasts over test year 2021 for grid cell with minimum and maximum RMSE values (LSTM).*

461

462 *Table 2: Emulator total average scores, aggregated over variables, time and space from the European and Global*
 463 *model testing.*

| Variable | Model | RMSE | | MAE | | ACC | |
|---------------|-------|--------------|--------------|--------------|--------------|--------------|--------------|
| | | Europe | Globe | Europe | Globe | Europe | Globe |
| All variables | XGB | 1.575 | 2.611 | 0.695 | 1.601 | 0.765 | 0.755 |
| | MLP | 1.486 | 1.699 | 0.832 | 1.189 | 0.728 | 0.569 |
| | LSTM | 0.918 | 2.252 | 0.526 | 1.787 | 0.925 | 0.647 |



464 *Table 3: Emulator average scores on soil water volume forecasts for the European subset, aggregated over space and*
 465 *time from the European and Global model testing.*

| Variable | Layer | Model | RMSE | | MAE | | ACC | |
|-------------------------|-------|-------|--------------|--------------|--------------|--------------|--------------|--------------|
| | | | Europe | Globe | Europe | Globe | Europe | Globe |
| Soil water volume | 1 | XGB | 0.013 | 0.015 | 0.01 | 0.01 | 0.908 | 0.92 |
| | | MLP | 0.019 | 0.029 | 0.015 | 0.023 | 0.856 | 0.791 |
| | | LSTM | 0.029 | 0.048 | 0.023 | 0.04 | 0.847 | 0.729 |
| | 2 | XGB | 0.011 | 0.012 | 0.008 | 0.009 | 0.901 | 0.884 |
| | | MLP | 0.019 | 0.023 | 0.014 | 0.018 | 0.789 | 0.77 |
| | | LSTM | 0.029 | 0.05 | 0.023 | 0.042 | 0.79 | 0.617 |
| | 3 | XGB | 0.015 | 0.014 | 0.011 | 0.01 | 0.789 | 0.777 |
| | | MLP | 0.02 | 0.02 | 0.017 | 0.016 | 0.576 | 0.667 |
| | | LSTM | 0.033 | 0.051 | 0.027 | 0.043 | 0.621 | 0.475 |

466

467 *Table 4: Emulators' mean scores on soil temperature forecasts for the European subset, aggregated over space and*
 468 *time.*

| Variable | Layer | Model | RMSE | | MAE | | ACC | |
|---------------------|-------|-------|--------------|--------------|--------------|--------------|--------------|--------------|
| | | | Europe | Globe | Europe | Globe | Europe | Globe |
| Soil temperature | 1 | XGB | 1.154 | 4.539 | 0.744 | 3.278 | 0.806 | 0.769 |
| | | MLP | 1.628 | 2.606 | 1.188 | 2.072 | 0.674 | 0.581 |
| | | LSTM | 0.931 | 3.152 | 0.682 | 2.626 | 0.938 | 0.735 |
| | 2 | XGB | 0.901 | 2.501 | 0.51 | 1.772 | 0.812 | 0.797 |
| | | MLP | 1.134 | 1.851 | 0.784 | 1.452 | 0.718 | 0.606 |
| | | LSTM | 0.734 | 2.87 | 0.541 | 2.4 | 0.928 | 0.699 |
| | 3 | XGB | 0.714 | 1.287 | 0.482 | 0.933 | 0.722 | 0.711 |
| | | MLP | 1.128 | 1.375 | 0.821 | 1.071 | 0.416 | 0.514 |
| | | LSTM | 1.141 | 3.466 | 0.918 | 3.002 | 0.598 | 0.406 |

469

470 *Table 5: Emulators' mean scores on snow cover forecasts for the European subset, aggregated over space and time.*

| Variable | Layer | Model | RMSE | | MAE | | ACC | |
|---------------|-------|-------|--------------|--------------|-------------|--------------|--------------|--------------|
| | | | Europe | Globe | Europe | Globe | Europe | Globe |
| Snow cover | top | XGB | 8.219 | 9.906 | 3.099 | 5.196 | 0.746 | 0.707 |
| | | MLP | 6.449 | 5.995 | 2.986 | 3.671 | 0.66 | 0.618 |
| | | LSTM | 3.526 | 6.127 | 1.47 | 4.357 | 0.877 | 0.698 |

471

472 **3.3 Forecast horizons**

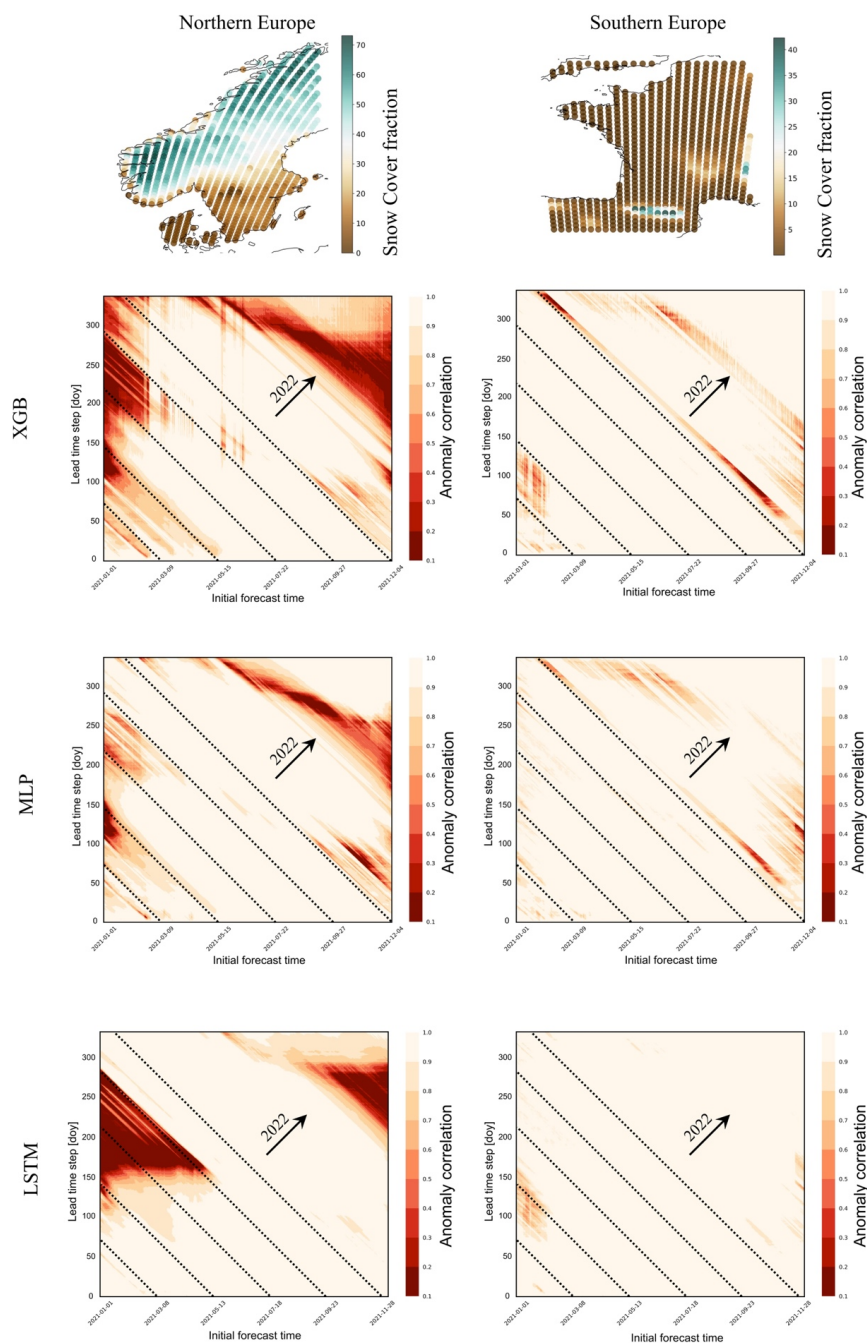


473 Forecast horizons were computed for two European regions, of which the northern one
474 represents the area of lowest emulators' skill (see figure 2, B.1-3) and the southern one an
475 area of stronger emulators' skill. Being strongly correlated with soil water volume, these two
476 regions differ specifically in their average snow cover fraction (see figure 3). The displayed
477 horizons were computed over all prognostic state variables simultaneously, while their
478 interpretation is related to horizons computed for prognostic state variables separately, for the
479 figures of which we refer to the Supplementary Material.

480 In the North, predictive skill depended on an interaction of how far ahead a prediction was
481 made (the lead time) and the day of year to which the prediction was made. In the best case,
482 the LSTM, summer predictions were poor (light patches in figure 3 heat maps), but only
483 when initialised in winter. Or, in other words, one can make good predictions starting in
484 winter, but not to summer. Vertical structures indicate a systematic model error that appears at
485 specific initialisation times and that is independent of prediction date, for example in XGB
486 forecasts that are initialized in May (see figure 3, northern region). Diagonal light structures
487 in the heat maps indicate a temporally consistent error and can be interpreted as physical
488 limits of system predictability, where the different initial forecast time doesn't affect model
489 scores.

490 All models show stronger limits in predictability and predictive ability in the northern
491 European region (see figure 3, left column). MLP and XGB struggled with representing
492 seasonal variation towards climatology at long lead times, while LSTM is strongly limited by
493 a systematic error in certain regions. Initializing the forecast the 1 January 2021, MLP drops
494 below an ACC of 80% repeatedly from initialization on and then to an ACC below 10% at the
495 beginning of May. LSTMs performance is more robust in the beginning of the year but
496 depletes strongly later to less than 10% ACC in mid May. On the one hand, this represents
497 two different characteristics of model errors: MLP forecasts for snow cover fraction are less
498 than zero for some grid cells while LSTM forecasts for snow cover fraction remain falsely at
499 very high levels for some grid cells, not predicting the snowmelt in May (see Supplementary
500 Material, S4.1). On the other hand, this represents a characteristic error due to change in
501 seasonality: the snowmelt in this region in May happens abruptly and all emulators
502 repeatedly over- or underpredict the exact date.

503

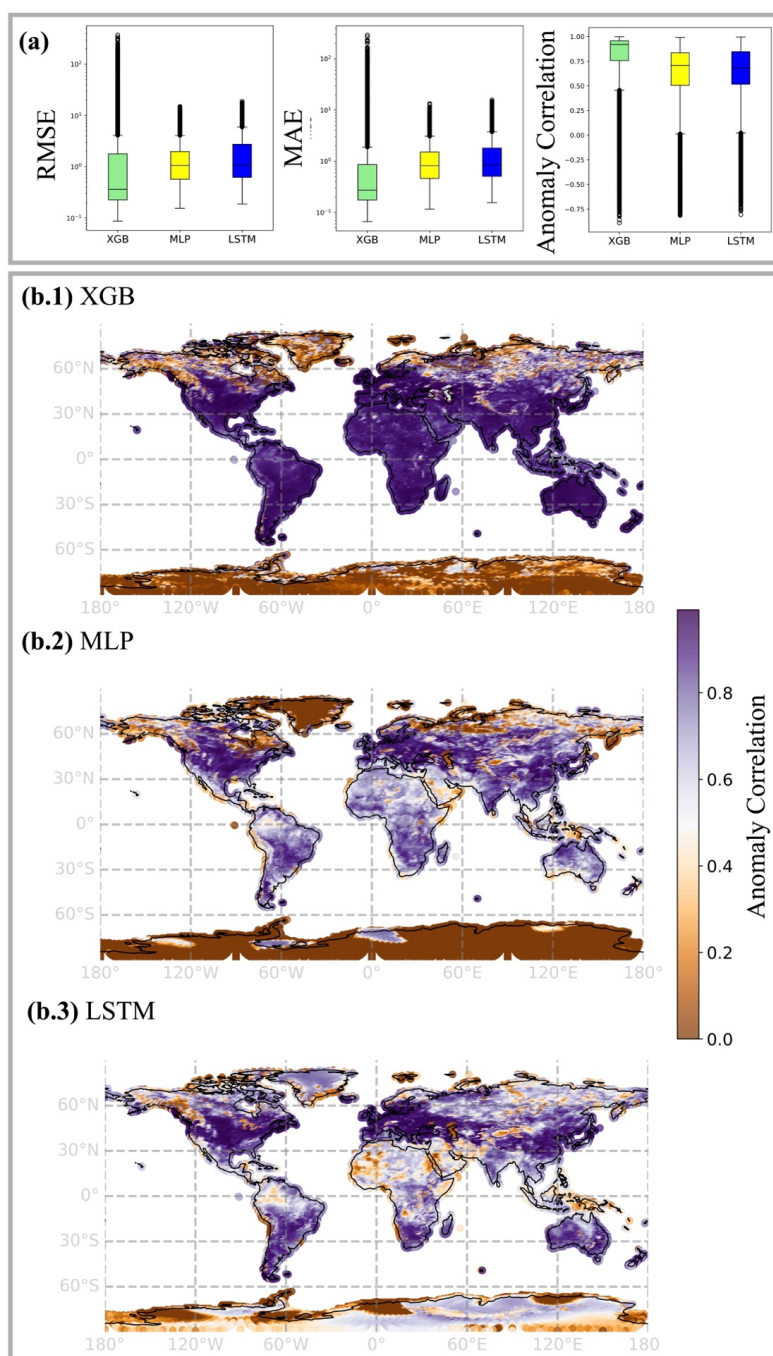


504

505 *Figure 3: Emulator forecast skill horizons in two European subregions, aggregated over prognostic state variables.*
506 *Scores are computed with the anomaly correlation coefficient (ACC) at 6-hourly lead times (y-axis) over approx. one*
507 *year, displayed as a function of the initial forecast time (x-axis). As horizon we define the time at which the forecast*
508 *has no value at all, i.e. when ACC is 0 (or below 10%). The diagonal dashed lines indicate the day of the test year 2021*
509 *as labelled on the x-axis, the arrows indicate where forecasts reach the second test year 2022.*



510



511
512
513
514

Figure 4: a) Total average scores, representing spatial variation among grid cells. B) Total average ACC in space. Note that ACC remained undefined for regions of low signal in snow cover and soil water volume, see Supplementary Material.



515 **4 Discussion**

516

517 In the comparative analysis of emulation approaches for land surface forecasting, three
518 primary models—LSTM (Long Short-Term Memory networks), MLP (Multi-Layer
519 Perceptrons), and XGB (Extreme Gradient Boosting)—have been evaluated to understand
520 their effectiveness across different operational scenarios. While all emulators achieved high
521 predictive scores, models differ in their demand of computational resources (Cui et al., 2021)
522 and each one offers unique advantages and faces distinct challenges, impacting their
523 suitability for various forecasting tasks. With this work we want to present the first steps
524 towards enabling quick offline experimentation on the land surface with ECMWF’s land
525 surface scheme ECLand and decreasing computational demands, i.e. in the coupled data
526 assimilation.

527

528 **4.1 Approximation of prognostic land surface states**

529

530 The total evaluation scores of our emulators indicate good agreement with ECLand
531 simulations. Among the seven individual prognostic land surface states, emulators achieve
532 notably different scores and in the transfer from the high-resolution continental to the low-
533 resolution global scale, their performance ranking change. On average, neural network
534 performances degrade towards the deeper soil layers, while XGB scores remain relatively
535 stable. Also, the neural networks scores drop in the extrapolation from continental to global
536 scale, while XGB scores also for this task remain constantly high.

537 In a way, these findings are not surprising. It is known that neural networks are highly
538 sensitive to selection bias (Grinsztajn et al., 2022) and tuning of hyper-parameters
539 (Bouthillier et al., 2021), suboptimal choices of which may destabilise variance in predictive
540 skill. Previous and systematic comparisons of XGB and deep neural networks have
541 demonstrated that neural networks can hardly be transferred to new data sets without
542 performance loss (Shwartz-Ziv & Armon, 2021). On tabular data, XGB still outperforms
543 neural networks in most cases (Grinsztajn et al., 2022), unless these models are strongly
544 regularized (Kadra et al., 2021). The disadvantage of neural networks might lay in the
545 rotational invariance of MLP-like architectures, due to which information about the data
546 orientation gets lost, as well as in their instability regarding uninformative input features
547 (Grinsztajn et al., 2022).



548 Inversely to expectations and preceding experiments, on the European data set relative to the
549 two other models the LSTM scored better in the upper layer soil temperatures than in
550 forecasting soil water volume and decreased in scores towards lower layers with slower
551 processes. For training on observations, the decreasing LSTM predictive accuracy for soil
552 moisture with lead time is discussed (Datta & Faroughi, 2023), but reasons arising from the
553 engineering side remain unclear. In an exemplary case of a single-objective, deterministic
554 streamflow forecast, a decrease in recurrent neural network performance has been related
555 with an increasing coefficient of variation (Guo et al., 2021). In our European subregions, the
556 signal-to-noise ratio of the prognostic state variables (computed as the averaged ratio of mean
557 and standard deviation) is up to ten times higher in soil temperature than in soil water volume
558 states (see Supplementary Material, S2.1). While a small signal of the latter may induce
559 instability in scores, it does not explain the decreasing performance towards deeper soil layers
560 with slow processes, where we expected an advantage of the long-term memory.
561 Stein's paradox tells us that joint optimization may lead to better results if the target is multi-
562 objective, but not if we are interested in single targets (James & Stein, 1992)(Sener & Koltun,
563 2018). While from a process perspective multi-objective scores are less meaningful than
564 single ones, this is what we opted for due to efficiency. The unweighted linear loss
565 combination might be suboptimal in finding effective parameters across all prognostic state
566 variables (Z. Chen et al., 2017)(Sener & Koltun, 2018), yet being strongly correlated, we
567 deemed their manual weighting inappropriate. An alternative to this provides adaptive loss
568 weighting with gradient normalisation (Z. Chen et al., 2017).

569

570 **4.2 Evaluation in time and space**

571 We used aggregated MAE and RMSE accuracies as a first assessment tool to conduct model
572 comparison, but score aggregation hides model specific spatio-temporal residual patterns.
573 Further, both scores are variance dependent, favouring low variability in model forecasts
574 even though this may not be representative of the system dynamic (Thorpe et al., 2013).
575 Assessing the forecast skill over time as the relative proximity to a subjectively chosen
576 benchmark helps disentangling areas of strengths and weaknesses in forecasting with the
577 emulators (Pappenberger et al., 2015). The naïve 6-hourly climatology as benchmark
578 highlights periods where emulators long-range forecasts on the test year are externally limited
579 by seasonality, i.e. system predictability, and where they are internally limited by model error,
580 i.e. the model's predictive ability. Applying this strategy in two exemplary European
581 subregions showed that all emulators struggle most in forecasting the period from late



582 summer to autumn, unless they are initialized in summer (see figure 3). Because forecast
583 quality is most strongly limited by snow cover (see Supplementary Material, A4.1), we
584 interpret this as the unpredictable start of snow fall in autumn. External predictability
585 limitations seem to affect the LSTM overall less than the two other models, and specifically
586 XGB drifts at long lead times.

587 From a geographical perspective inferred from the continental scale, emulators struggle in
588 forecasting prognostic state variables in regions with complicated orography and strong
589 environmental gradients. XGB scores vary seemingly random in space, while neural
590 networks scores exhibit spatial autocorrelation. A meaningful inference about this, however,
591 can only be conducted in assessing model sensitivities to physiographic and meteorological
592 fields through gradients and partial dependencies. While the goal of this work is to introduce
593 our approach to emulator development, we envision this for follow-up analyses.

594

595 **4.3 Emulation with memory mechanisms**

596

597 Without much tuning, XGB challenges both LSTM and MLP for nearly all variables (see
598 tables 2-4). In training on observations for daily short-term and real-time rainfall-runoff
599 prediction, XGB and LightXGB were shown before to equally performed as, or outperformed
600 LSTMs (X. Chen et al., 2020)(Cui et al., 2021). Nevertheless, models with memory
601 mechanism such as the encoder-decoder LSTM remain a promising approach for land surface
602 forecasting regarding their differentiability (Hatfield et al., 2021), their flexible extension of
603 lead times, for exploring the effect of long-term dependencies or for inference from the
604 context vector that may help identifying the process relevant climate fields (Lees et al.,
605 2022).

606 In our LSTM architecture, we assume that our model is well defined in that the context vector
607 perfectly informs the hidden decoder states. If that assumption is violated, potential strategies
608 are to create a skip-connection between context vector and forecast head, or to consider input
609 of time-lagged variables or self-attention mechanisms (X. Chen et al., 2020). With attention,
610 the context vector becomes a weighted sum of alignments that relates neighbouring positions
611 of a sequence, a feature that could be leveraged for forecasting quick processes such as snow
612 cover or top-level soil water volume.

613 Comparing average predictive accuracies across different training lead times indicates that
614 training at longer lead times may enhance short-term accuracy of the LSTM at the cost of
615 training runtime (see Supplementary Material, S2). A superficial exploration of encoder



616 length indicates no visible improvement on target accuracies if not a positive tendency
617 towards shorter sequences. This needs an extended analysis for understanding, yet without a
618 significant improvement by increased sequence length, GRU cells might provide a simplified
619 and less parameterized alternative to LSTM cells. They were found to perform equally well
620 on streamflow forecast performance before, while reaching higher operational speed (Guo et
621 al., 2021).

622

623 **4.4 Emulators in application**

624

625 LSTM networks with a decoder structure are valued for their flexible and fast lead time
626 evaluation, which is crucial in applications where forecast intervals are not consistent. The
627 structure of LSTM is well-suited for handling sequential data, allowing it to perform
628 effectively over different temporal scales (Hochreiter & Schmidhuber, 1997). They provide
629 access to gradients, which facilitates inference, optimization and usage for coupled data
630 assimilation (Hatfield et al., 2021). Nevertheless, the complexity of LSTMs introduces
631 disadvantages: Despite their high evaluation speed and accuracy under certain conditions,
632 they require significant computational resources and long training times. They are also highly
633 sensitive to hyperparameters, making them challenging to tune and slow to train, especially
634 with large datasets.

635 MLP models stand out for their implementation, training and evaluation speed with yet
636 rewarding accuracy, making them a favourable choice for scenarios that require rapid model
637 deployment. They are tractable and easy to handle, with a straightforward setup that is less
638 demanding computationally than more complex models. MLPs also allow for access to
639 gradients, aiding in incremental improvements during training and quick inference (Hatfield
640 et al., 2021). Despite these advantages, MLPs face challenges with memory scaling during
641 training at fixed lead times, which can hinder their applicability in large-scale or high-
642 resolution forecasting tasks.

643 XGB models are highly regarded for their robust performance with minimal tuning,
644 achieving high accuracy not only in sample applications, but also in transfer to unseen
645 problems (Shwartz-Ziv & Armon, 2021) (Grinsztajn et al., 2022). Their simplicity makes
646 them easy to handle, even for users with limited technical expertise in machine learning.
647 However, the slow evaluation speed of XGB becomes apparent as dataset complexity and
648 size increase. Although generally more interpretable than deep machine learning tools, XGB



649 is not differentiable, limiting its application in coupled data assimilation (Hatfield et al.,
650 2021) even though research on differentiable trees is ongoing (Popov et al., 2019).

651

652 **5 Conclusion**

653

654 In conclusion, the choice between LSTM, MLP, and XGB models for land surface forecasting
655 depends largely on the specific requirements of the application, including the need for speed,
656 accuracy, and ease of use. Each model's computational demands, flexibility, and operational
657 overhead must be carefully considered to optimize performance and applicability in diverse
658 forecasting environments. When it comes to accuracy, combined model ensembles of XGB
659 and neural networks have been shown to yield the best results (Shwartz-Ziv & Armon, 2021),
660 but accuracy alone will not determine a single best approach (Bouthillier et al., 2021). Our
661 comparative assessment underscores the importance of selecting the appropriate emulation
662 approach based on a clear understanding of each model's strengths and limitations in relation
663 to the forecasting tasks at hand. By developing the emulators for ECMWF's numerical land
664 surface scheme ECLand, we path the way towards a physics-informed ML-based land surface
665 model that on the long run can be parametrized with observations and provide a pretrained
666 model suite to improve land surface forecasts.

667

668 **Code and data availability**

669 Code for this analysis can be found here: [https://github.com/MWesselkamp/land-surface-](https://github.com/MWesselkamp/land-surface-emulation)
670 [emulation](https://github.com/MWesselkamp/land-surface-emulation). Data is available on request.

671 **Author contribution**

672 MW, MCha, EP, FP and GB conceived the study. MW and EP conducted the analysis. MW,
673 MCha, MK, EP discussed and took technical decisions. SB advised on process decisions.
674 MW, MCho and FP wrote the manuscript. MW, MCha, EP, MCho, SB, MK, CFD, FP
675 reviewed the analysis and/or manuscript.

676 **Competing interest**

677 The authors declare that they have no conflict of interest.

678 **Acknowledgements**

679 This work profited from discussion with Linus Magnusson, Sina R. K. Farhadi and Karan
680 Ruparell and many more. MW thankfully acknowledges ECMWF for providing two research



681 visit stipendiates over the course of the collaboration. ChatGPT version 4.0 was used for
682 coding support.

683

684 **References**

685

686 Akiba, T., Sano, S., Yanase, T., Ohta, T., & Koyama, M. (2019). Optuna: A Next-generation

687 Hyperparameter Optimization Framework. *Proceedings of the 25th ACM SIGKDD*

688 *International Conference on Knowledge Discovery & Data Mining*, 2623–2631.

689 <https://doi.org/10.1145/3292500.3330701>

690 Baker, E., Harper, A. B., Williamson, D., & Challenor, P. (2022). Emulation of high-

691 resolution land surface models using sparse Gaussian processes with

692 application to JULES. *Geoscientific Model Development*, 15(5), 1913–1929.

693 <https://doi.org/10.5194/gmd-15-1913-2022>

694 Balsamo, G., Boussetta, S., Dutra, E., Beljaars, A., & Viterbo, P. (2011). *Evolution of land-*

695 *surface processes in the IFS*. 127.

696 Bassi, A., Höge, M., Mira, A., Fenicia, F., & Albert, C. (2024). *Learning Landscape*

697 *Features from Streamflow with Autoencoders*. [https://doi.org/10.5194/hess-](https://doi.org/10.5194/hess-2024-47)

698 2024-47

699 Bengtsson, L. K., Magnusson, L., & Källén, E. (2008). Independent Estimations of the

700 Asymptotic Variability in an Ensemble Forecast System. *Monthly Weather*

701 *Review*, 136(11), 4105–4112. <https://doi.org/10.1175/2008MWR2526.1>

702 Bi, K., Xie, L., Zhang, H., Chen, X., Gu, X., & Tian, Q. (2022). *Pangu-Weather: A 3D High-*

703 *Resolution Model for Fast and Accurate Global Weather Forecast*.

704 <https://doi.org/10.48550/ARXIV.2211.02556>



- 705 Boussetta, S., Balsamo, G., Arduini, G., Dutra, E., McNorton, J., Choulga, M., Agustí-
706 Panareda, A., Beljaars, A., Wedi, N., Muñoz-Sabater, J., De Rosnay, P., Sandu, I.,
707 Hadade, I., Carver, G., Mazzetti, C., Prudhomme, C., Yamazaki, D., & Zsoter, E.
708 (2021). ECLand: The ECMWF land surface modelling system. *Atmosphere*, 12(6),
709 723. <https://doi.org/10.3390/atmos12060723>
- 710 Bouthillier, X., Delaunay, P., Bronzi, M., Trofimov, A., Nichyporuk, B., Szeto, J., Sepah, N.,
711 Raff, E., Madan, K., Voleti, V., Kahou, S. E., Michalski, V., Serdyuk, D., Arbel, T.,
712 Pal, C., Varoquaux, G., & Vincent, P. (2021). *Accounting for Variance in Machine*
713 *Learning Benchmarks* (arXiv:2103.03098). arXiv. <http://arxiv.org/abs/2103.03098>
- 714 Chantry, M., Hatfield, S., Duben, P., Polichtchouk, I., & Palmer, T. (2021). *Machine*
715 *learning emulation of gravity wave drag in numerical weather forecasting*.
716 <https://doi.org/10.48550/ARXIV.2101.08195>
- 717 Chen, T., & Guestrin, C. (2016). *XGBoost: A Scalable Tree Boosting System*.
718 <https://doi.org/10.48550/ARXIV.1603.02754>
- 719 Chen, X., Huang, J., Han, Z., Gao, H., Liu, M., Li, Z., Liu, X., Li, Q., Qi, H., & Huang, Y.
720 (2020). The importance of short lag-time in the runoff forecasting model based
721 on long short-term memory. *Journal of Hydrology*, 589, 125359.
722 <https://doi.org/10.1016/j.jhydrol.2020.125359>
- 723 Chen, Z., Badrinarayanan, V., Lee, C.-Y., & Rabinovich, A. (2017). *GradNorm: Gradient*
724 *Normalization for Adaptive Loss Balancing in Deep Multitask Networks*.
725 <https://doi.org/10.48550/ARXIV.1711.02257>
- 726 Choulga, M., Kourzeneva, E., Balsamo, G., Boussetta, S., & Wedi, N. (2019). Upgraded
727 global mapping information for earth system modelling: An application to



- 728 surface water depth at the ECMWF. *Hydrology and Earth System Sciences*,
- 729 23(10), 4051–4076. <https://doi.org/10.5194/hess-23-4051-2019>
- 730 Cui, Z., Qing, X., Chai, H., Yang, S., Zhu, Y., & Wang, F. (2021). Real-time rainfall-runoff
- 731 prediction using light gradient boosting machine coupled with singular spectrum
- 732 analysis. *Journal of Hydrology*, 603, 127124.
- 733 <https://doi.org/10.1016/j.jhydrol.2021.127124>
- 734 Datta, P., & Faroughi, S. A. (2023). A multihead LSTM technique for prognostic prediction
- 735 of soil moisture. *Geoderma*, 433, 116452.
- 736 <https://doi.org/10.1016/j.geoderma.2023.116452>
- 737 De Rosnay, P., Balsamo, G., Albergel, C., Muñoz-Sabater, J., & Isaksen, L. (2014).
- 738 Initialisation of Land Surface Variables for Numerical Weather Prediction.
- 739 *Surveys in Geophysics*, 35(3), 607–621. <https://doi.org/10.1007/s10712-012->
- 740 9207-x
- 741 ECMWF. (n.d.). Forecast User Guide. In *Anomaly Correlation Coefficient*. Retrieved 4
- 742 July 2024, from
- 743 <https://confluence.ecmwf.int/display/FUG/Section+6.2.2+Anomaly+Correlation>
- 744 +Coefficient
- 745 ECMWF. (2017). *IFS Documentation CY43R3 - Part IV: Physical processes*.
- 746 <https://doi.org/10.21957/EFYK72KL>
- 747 ECMWF. (2023). *IFS Documentation CY48R1 - Part IV: Physical Processes*.
- 748 <https://doi.org/10.21957/02054F0FBF>
- 749 Fer, I., Kelly, R., Moorcroft, P. R., Richardson, A. D., Cowdery, E. M., & Dietze, M. C.
- 750 (2018). Linking big models to big data: Efficient ecosystem model calibration



- 751 through Bayesian model emulation. *Biogeosciences*, 15(19), 5801–5830.
- 752 <https://doi.org/10.5194/bg-15-5801-2018>
- 753 Girshick, R. (2015). *Fast R-CNN*. <https://doi.org/10.48550/ARXIV.1504.08083>
- 754 Goodfellow, I., Bengio, Y., & Courville, A. (2016). *Deep learning*. The MIT Press.
- 755 Grinsztajn, L., Oyallon, E., & Varoquaux, G. (2022). *Why do tree-based models still*
- 756 *outperform deep learning on tabular data?* (Version 1). arXiv.
- 757 <https://doi.org/10.48550/ARXIV.2207.08815>
- 758 Guo, Y., Yu, X., Xu, Y.-P., Chen, H., Gu, H., & Xie, J. (2021). AI-based techniques for multi-
- 759 step streamflow forecasts: Application for multi-objective reservoir operation
- 760 optimization and performance assessment. *Hydrol. Earth Syst. Sci.*
- 761 Hatfield, S., Chantry, M., Dueben, P., Lopez, P., Geer, A., & Palmer, T. (2021). Building
- 762 Tangent-Linear and Adjoint Models for Data Assimilation With Neural Networks.
- 763 *Journal of Advances in Modeling Earth Systems*, 13(9), e2021MS002521.
- 764 <https://doi.org/10.1029/2021MS002521>
- 765 Hersbach, H., Bell, B., Berrisford, P., Hirahara, S., Horányi, A., Muñoz-Sabater, J.,
- 766 Nicolas, J., Peubey, C., Radu, R., Schepers, D., Simmons, A., Soci, C., Abdalla,
- 767 S., Abellan, X., Balsamo, G., Bechtold, P., Biavati, G., Bidlot, J., Bonavita, M., ...
- 768 Thépaut, J. (2020). The ERA5 global reanalysis. *Quarterly Journal of the Royal*
- 769 *Meteorological Society*, 146(730), 1999–2049. <https://doi.org/10.1002/qj.3803>
- 770 Hochreiter, S., & Schmidhuber, J. (1997). Long Short-Term Memory. *Neural*
- 771 *Computation*, 9(8), 1735–1780. <https://doi.org/10.1162/neco.1997.9.8.1735>
- 772 James, W., & Stein, C. (1992). Estimation with Quadratic Loss. In S. Kotz & N. L. Johnson
- 773 (Eds.), *Breakthroughs in Statistics* (pp. 443–460). Springer New York.
- 774 https://doi.org/10.1007/978-1-4612-0919-5_30



- 775 Kadra, A., Lindauer, M., Hutter, F., & Grabocka, J. (2021). *Well-tuned Simple Nets Excel*
776 *on Tabular Datasets* (arXiv:2106.11189). arXiv. <http://arxiv.org/abs/2106.11189>
- 777 Keisler, R. (2022). *Forecasting Global Weather with Graph Neural Networks*
778 (arXiv:2202.07575). arXiv. <http://arxiv.org/abs/2202.07575>
- 779 Kimpson, T., Choulga, M., Chantry, M., Balsamo, G., Boussetta, S., Dueben, P., &
780 Palmer, T. (2023). Deep learning for quality control of surface physiographic
781 fields using satellite Earth observations. *Hydrology and Earth System Sciences*,
782 27(24), 4661–4685. <https://doi.org/10.5194/hess-27-4661-2023>
- 783 Kingma, D. P., & Ba, J. (2017). *Adam: A Method for Stochastic Optimization*.
- 784 Kratzert, F., Herrnegger, M., Klotz, D., Hochreiter, S., & Klambauer, G. (2019).
785 *NeuralHydrology—Interpreting LSTMs in Hydrology*.
786 <https://doi.org/10.48550/ARXIV.1903.07903>
- 787 Kratzert, F., Klotz, D., Shalev, G., Klambauer, G., Hochreiter, S., & Nearing, G. (2019).
788 Towards learning universal, regional, and local hydrological behaviors via
789 machine learning applied to large-sample datasets. *Hydrology and Earth System*
790 *Sciences*, 23(12), 5089–5110. <https://doi.org/10.5194/hess-23-5089-2019>
- 791 Lam, R., Sanchez-Gonzalez, A., Willson, M., Wirnsberger, P., Fortunato, M., Alet, F.,
792 Ravuri, S., Ewalds, T., Eaton-Rosen, Z., Hu, W., Merose, A., Hoyer, S., Holland, G.,
793 Vinyals, O., Stott, J., Pritzel, A., Mohamed, S., & Battaglia, P. (2023). Learning
794 skillful medium-range global weather forecasting. *Science*, 382(6677), 1416–
795 1421. <https://doi.org/10.1126/science.adi2336>
- 796 Lang, S., Alexe, M., Chantry, M., Dramsch, J., Pinault, F., Raoult, B., Clare, M. C. A.,
797 Lessig, C., Maier-Gerber, M., Magnusson, L., Bouallègue, Z. B., Nemesio, A. P.,
798 Dueben, P. D., Brown, A., Pappenberger, F., & Rabier, F. (2024). *AIFS - ECMWF's*



- 799 *data-driven forecasting system* (arXiv:2406.01465). arXiv.
- 800 <http://arxiv.org/abs/2406.01465>
- 801 Lees, T., Reece, S., Kratzert, F., Klotz, D., Gauch, M., De Bruijn, J., Kumar Sahu, R., Greve,
802 P., Slater, L., & Dadson, S. J. (2022). Hydrological concept formation inside long
803 short-term memory (LSTM) networks. *Hydrology and Earth System Sciences*,
804 26(12), 3079–3101. <https://doi.org/10.5194/hess-26-3079-2022>
- 805 Li, L., Carver, R., Lopez-Gomez, I., Sha, F., & Anderson, J. (2023). *SEEDS: Emulation of*
806 *Weather Forecast Ensembles with Diffusion Models*.
807 <https://doi.org/10.48550/ARXIV.2306.14066>
- 808 Machac, D., Reichert, P., & Albert, C. (2016). Emulation of dynamic simulators with
809 application to hydrology. *Journal of Computational Physics*, 313, 352–366.
810 <https://doi.org/10.1016/j.jcp.2016.02.046>
- 811 Meyer, D., Grimmond, S., Dueben, P., Hogan, R., & Van Reeuwijk, M. (2022). Machine
812 Learning Emulation of Urban Land Surface Processes. *Journal of Advances in*
813 *Modeling Earth Systems*, 14(3), e2021MS002744.
814 <https://doi.org/10.1029/2021MS002744>
- 815 Mironov, D., & Helmert, J. (n.d.). *Parameterization of Lakes in NWP and Climate Models*.
- 816 Muñoz-Sabater, J., Dutra, E., Agustí-Panareda, A., Albergel, C., Arduini, G., Balsamo, G.,
817 Boussetta, S., Choulga, M., Harrigan, S., Hersbach, H., Martens, B., Miralles, D.
818 G., Piles, M., Rodríguez-Fernández, N. J., Zsoter, E., Buontempo, C., & Thépaut,
819 J.-N. (2021). ERA5-Land: A state-of-the-art global reanalysis dataset for land
820 applications. *Earth System Science Data*, 13(9), 4349–4383.
821 <https://doi.org/10.5194/essd-13-4349-2021>



- 822 Nath, S., Lejeune, Q., Beusch, L., Seneviratne, S. I., & Schleussner, C.-F. (2022).
823 MESMER-M: An Earth system model emulator for spatially resolved monthly
824 temperature. *Earth System Dynamics*, 13(2), 851–877.
825 <https://doi.org/10.5194/esd-13-851-2022>
- 826 Nearing, G., Cohen, D., Dube, V., Gauch, M., Gilon, O., Harrigan, S., Hassidim, A., Klotz,
827 D., Kratzert, F., Metzger, A., Nevo, S., Pappenberger, F., Prudhomme, C., Shalev,
828 G., Shenzis, S., Tekalign, T. Y., Weitzner, D., & Matias, Y. (2024). Global prediction
829 of extreme floods in ungauged watersheds. *Nature*, 627(8004), 559–563.
830 <https://doi.org/10.1038/s41586-024-07145-1>
- 831 Ozaki, Y., Tanigaki, Y., Watanabe, S., Nomura, M., & Onishi, M. (2022). Multiobjective
832 Tree-Structured Parzen Estimator. *Journal of Artificial Intelligence Research*, 73,
833 1209–1250. <https://doi.org/10.1613/jair.1.13188>
- 834 Pappenberger, F., Ramos, M. H., Cloke, H. L., Wetterhall, F., Alfieri, L., Bogner, K.,
835 Mueller, A., & Salamon, P. (2015). How do I know if my forecasts are better?
836 Using benchmarks in hydrological ensemble prediction. *Journal of Hydrology*,
837 522, 697–713. <https://doi.org/10.1016/j.jhydrol.2015.01.024>
- 838 Popov, S., Morozov, S., & Babenko, A. (2019). *Neural Oblivious Decision Ensembles for*
839 *Deep Learning on Tabular Data* (Version 2). arXiv.
840 <https://doi.org/10.48550/ARXIV.1909.06312>
- 841 Reichstein, M., Camps-Valls, G., Stevens, B., Jung, M., Denzler, J., Carvalhais, N., &
842 Prabhat. (2019). Deep learning and process understanding for data-driven Earth
843 system science. *Nature*, 566(7743), 195–204. [https://doi.org/10.1038/s41586-](https://doi.org/10.1038/s41586-019-0912-1)
844 [019-0912-1](https://doi.org/10.1038/s41586-019-0912-1)



- 845 Sener, O., & Koltun, V. (2018). *Multi-Task Learning as Multi-Objective Optimization*
846 (Version 2). arXiv. <https://doi.org/10.48550/ARXIV.1810.04650>
- 847 Shwartz-Ziv, R., & Armon, A. (2021). *Tabular Data: Deep Learning is Not All You Need.*
848 <https://doi.org/10.48550/ARXIV.2106.03253>
- 849 Thorpe, A., Bauer, P., Magnusson, L., & Richardson, D. (2013). *An evaluation of recent*
850 *performance of ECMWF's forecasts.* <https://doi.org/10.21957/HI1EEKTR>
- 851 Van Katwyk, P., Fox-Kemper, B., Seroussi, H., Nowicki, S., & Bergen, K. J. (2023). A
852 Variational LSTM Emulator of Sea Level Contribution From the Antarctic Ice
853 Sheet. *Journal of Advances in Modeling Earth Systems*, 15(12), e2023MS003899.
854 <https://doi.org/10.1029/2023MS003899>
- 855 Viterbo, P. (2002). *Land_surface_processes.*
- 856 Wesselkamp, M., Moser, N., Kalweit, M., Boedecker, J., & Dormann, C. F. (2022).
857 *Process-guidance improves predictive performance of neural networks for*
858 *carbon turnover in ecosystems.* <https://doi.org/10.48550/ARXIV.2209.14229>
- 859 Zwart, J. A., Oliver, S. K., Watkins, W. D., Sadler, J. M., Appling, A. P., Corson-Dosch, H.
860 R., Jia, X., Kumar, V., & Read, J. S. (2023). Near-term forecasts of stream
861 temperature using deep learning and data assimilation in support of
862 management decisions. *JAWRA Journal of the American Water Resources*
863 *Association*, 59(2), 317–337. <https://doi.org/10.1111/1752-1688.13093>
864